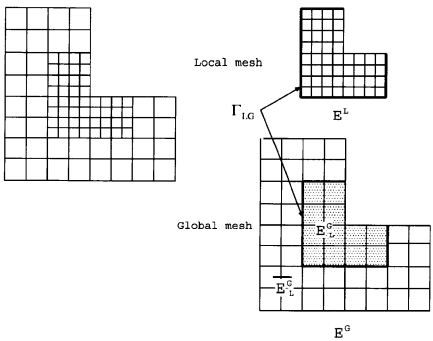

Fig. 2.4 *A composite mesh (left) and decomposition of the elements into the subsets for each level (right).*

for the nodal values $\boldsymbol{\phi}^L$ on the local mesh Ω^L by

$$\phi^L = \boldsymbol{N}^L \cdot \boldsymbol{\phi}^L = \sum_{i \in \Omega^L} N_i^L \phi_i^L. \tag{2.18}$$

Here, $\{N_i^L\}_{i \in \Omega^L}$ are the shape functions on Ω^L. We use similar notation, $\boldsymbol{N}^G, N_i^G, \phi^G$, etc., for the global mesh Ω^G.

Under the above definitions, we define an energy functional for a given nodal function $\boldsymbol{\phi} = \{\boldsymbol{\phi}^L, \boldsymbol{\phi}^G\}$ on the composite mesh by

$$\begin{aligned}\mathcal{E}(\phi) &= \int_{\Omega_L} \frac{1}{2} \nabla \phi^L \cdot \boldsymbol{\sigma} \nabla \phi^L d\Omega + \int_{\overline{\Omega_L^G}} \frac{1}{2} \nabla \phi^G \cdot \boldsymbol{\sigma} \nabla \phi^G d\Omega + \int_{\Omega_H} \nabla \phi^L \cdot \boldsymbol{\sigma}_\mathrm{i} \nabla V_\mathrm{m}^L d\Omega \\ &= \sum_{e^L \in E^L} \int_{e^L} \frac{1}{2} \nabla \boldsymbol{N}^L \boldsymbol{\phi}^L \cdot \boldsymbol{\sigma} \nabla \boldsymbol{N}^L \boldsymbol{\phi}^L d\Omega + \sum_{e^G \in \overline{E_L^G}} \int_{e^G} \frac{1}{2} \nabla \boldsymbol{N}^G \boldsymbol{\phi}^G \cdot \boldsymbol{\sigma} \nabla \boldsymbol{N}^G \boldsymbol{\phi}^G d\Omega \\ &\quad + \sum_{e^L \in E_H^L} \int_{e^L} \nabla \boldsymbol{N}^L \boldsymbol{\phi}^L \cdot \boldsymbol{\sigma}_\mathrm{i} \nabla \boldsymbol{N}^L \boldsymbol{V}_\mathrm{m}^L d\Omega.\end{aligned} \tag{2.19}$$

Here, E_H^L are elements in E^L that lie in Ω_H. Note that we assume that Ω_H is composed of a subset of E^L. Now, we impose the following constraint conditions on the variational problem:

$$\boldsymbol{\phi}^L = \boldsymbol{I}_G^L \boldsymbol{\phi}^G \text{ on } \Gamma_{LG}. \tag{2.20}$$

Here, $\boldsymbol{I}_G^L$ is an interpolation operator from Ω^G to Ω^L and Γ_{LG} is the set of nodes situated at the interface boundaries of Ω^L with Ω^G. Note that Γ_{LG} is not necessarily identical to the boundary of Ω^L. As shown by the thick lines in the diagram on the right of Figure 2.4, the intersections of $\partial\Omega$ and $\partial\Omega_L$ are not contained in Γ_{LG}. The weights of the interpolation are determined by the shape functions $\boldsymbol{N}^G$ on Ω^G.

Let $\dot{\Omega}_L^G$ be the set of internal nodes in Ω_L^G where the nodes on Γ_{LG} are excluded. The components of $\boldsymbol{\phi}^G$ on $\dot{\Omega}_L^G$ do not affect the functional in (2.19). However, these components are set identical to $\boldsymbol{\phi}^L$ by an injection of the solution as described in section 3.1.

The following equation is obtained by applying the Lagrange multiplier method to the variational problem (2.19):

$$\begin{aligned}\int_{\Omega^L} \nabla w^L \cdot \boldsymbol{\sigma} \nabla \phi^L d\Omega + \int_{\overline{\Omega_L^G}} \nabla w^G \cdot \boldsymbol{\sigma} \nabla \phi^G d\Omega + \int_{\Omega_H^L} \nabla w^L \cdot \boldsymbol{\sigma}_{\mathrm{i}} \nabla V_{\mathrm{m}}^L d\Omega \\ + \left(\boldsymbol{w}^L - \boldsymbol{I}_G^L \boldsymbol{w}^G\right)_{\Gamma_{LG}} \cdot \boldsymbol{\lambda} + \boldsymbol{w}_\lambda \cdot \left(\boldsymbol{\phi}^L - \boldsymbol{I}_G^L \boldsymbol{\phi}^G\right)_{\Gamma_{LG}} = 0.\end{aligned} \tag{2.21}$$

Here, w^L and w^G are arbitrary test functions equal to zero on Γ_P. The brackets $(\,)_{\Gamma_{LG}}$ denote the restriction of a vector to the nodes on Γ_{LG}, $\boldsymbol{\lambda}$ is the Lagrange multiplier defined at the nodes on Γ_{LG}, and $\boldsymbol{w}_\lambda$ is a test vector associated with the Lagrange multiplier. Equation (2.21) can be rewritten in matrix form as follows:

$$\begin{aligned}\boldsymbol{w}^L \cdot \left(\boldsymbol{K}^L \boldsymbol{\phi}^L + \boldsymbol{K}_{\mathrm{i}}^L \boldsymbol{V}_{\mathrm{m}}^L\right) + \boldsymbol{w}^G \cdot \overline{\boldsymbol{K}_L^G} \boldsymbol{\phi}^G + \left(\boldsymbol{w}^L - \boldsymbol{I}_G^L \boldsymbol{w}^G\right)_{\Gamma_{LG}} \cdot \boldsymbol{\lambda} \\ + \boldsymbol{w}_\lambda \cdot \left(\boldsymbol{\phi}^L - \boldsymbol{I}_G^L \boldsymbol{\phi}^G\right)_{\Gamma_{LG}} = 0.\end{aligned} \tag{2.22}$$

Here, the matrices $\boldsymbol{K}^L$, $\boldsymbol{K}_{\mathrm{i}}^L$, and $\overline{\boldsymbol{K}_L^G}$ are obtained by superposing element matrices as

$$\boldsymbol{K}^L = \sum_{e^L \in E^L} \boldsymbol{K}^L(e^L), \tag{2.23}$$

$$\boldsymbol{K}_{\mathrm{i}}^L = \sum_{e^L \in E^L} \boldsymbol{K}_{\mathrm{i}}^L(e^L), \tag{2.24}$$

$$\overline{\boldsymbol{K}_L^G} = \sum_{e^G \in \overline{E_L^G}} \boldsymbol{K}^G(e^G), \tag{2.25}$$

where the element matrices are given by

$$\boldsymbol{K}^L(e^L)_{ij} = \int_{e^L} \nabla N_i^L \cdot \boldsymbol{\sigma} \nabla N_j^L d\Omega, \tag{2.26}$$

$$\boldsymbol{K}_{\mathrm{i}}^L(e^L)_{ij} = \int_{e^L} \nabla N_i^L \cdot \boldsymbol{\sigma}_{\mathrm{i}} \nabla N_j^L d\Omega, \tag{2.27}$$

$$\boldsymbol{K}^G(e^G)_{ij} = \int_{e^G} \nabla N_i^G \cdot \boldsymbol{\sigma} \nabla N_j^G d\Omega \tag{2.28}$$

for nodes i and j of elements e^L and e^G. From (2.22), we finally obtain

$$\boldsymbol{K}^L \boldsymbol{\phi}^L + \boldsymbol{K}_{\mathrm{i}}^L \boldsymbol{V}_{\mathrm{m}}^L + \boldsymbol{\lambda} = \boldsymbol{0} \text{ on } \Omega^L \backslash \Gamma_P, \tag{2.29}$$

$$\overline{\boldsymbol{K}_L^G} \boldsymbol{\phi}^G - \boldsymbol{I}_G^{L\,T} \boldsymbol{\lambda} = \boldsymbol{0} \text{ on } \overline{\Omega_L^G} \backslash \Gamma_P, \tag{2.30}$$

$$\boldsymbol{\phi}^L = \boldsymbol{\phi}_{\mathrm{p}} \text{ and } \boldsymbol{\phi}^G = \boldsymbol{\phi}_{\mathrm{p}} \text{ on } \Gamma_P,$$

with the constraint condition in (2.20). In section 3.1, we derive a local-global multigrid solution algorithm for (2.29) and (2.30). From (2.29), the nodal values of the Lagrange multiplier at Γ_{LG} can be interpreted as the electric currents from the local

mesh. In other words, the electric currents passing through the element surface from the local mesh elements are integrated on the local nodes at the interface. In (2.30), these nodal values of the currents from the local mesh are distributed by $\boldsymbol{I}_G^{L^T}$ to the global mesh nodes at Γ_{LG}, and they are balanced with the currents from the global mesh elements in $\overline{E_L^G}$. In this way, the current balance is ensured at the interface. In the next section, we will see that this results in the conservation of the electric currents passing through the electrodes.

2.3. Conservation Properties of the Electric Currents Passing through the Electrodes. For simplicity, at first we assume that the boundaries Γ_P of the electrodes do not intersect with the interface boundary Γ_{LG}. Later, this condition is relaxed to some extent. The above assumption implies that the nodes on Γ_P are exclusively divided into local and global sections:

$$\Gamma_P = \Gamma_P^L \cup \Gamma_P^G. \tag{2.31}$$

We define the nodal residual components at nodes $i \in \Gamma_P^L$ and $j \in \Gamma_P^G$ by

$$r_i^L = -\int_{\Omega^L} \nabla N_i^L \cdot (\boldsymbol{\sigma} \nabla \phi^L + \boldsymbol{\sigma}_{\mathrm{i}} \nabla V_{\mathrm{m}}^L) d\Omega = -(\boldsymbol{K}^L \boldsymbol{\phi}^L + \boldsymbol{K}_{\mathrm{i}}^L \boldsymbol{V}_{\mathrm{m}}^L)_i, \ i \in \Gamma_P^L, \tag{2.32}$$

$$r_j^G = -\int_{\overline{\Omega_L^G}} \nabla N_j^G \cdot \boldsymbol{\sigma} \nabla \phi^G d\Omega = -(\overline{\boldsymbol{K}_L^G} \boldsymbol{\phi}^G)_j, \ j \in \Gamma_P^G. \tag{2.33}$$

The conservation law through the entire domain Ω in the finite element context is stated below.

THEOREM 2.2. *Assume that* $\{\phi^L, \phi^G\}$ *is the finite element solution to* (2.21). *Then*

$$\sum_{i \in \Gamma_P^L} r_i^L + \sum_{j \in \Gamma_P^G} r_j^G = 0. \tag{2.34}$$

Proof. For the local and global meshes, let us define the following test functions:

$$w^L = 1 - \sum_{i \in \Gamma_P^L} N_i^L, \tag{2.35}$$

$$w^G = 1 - \sum_{j \in \Gamma_P^G} N_j^G. \tag{2.36}$$

From the assumption on Γ_P, $\boldsymbol{w}^L \equiv 1$ on Γ_{LG} and $\boldsymbol{w}^G \equiv 1$ on Γ_{LG}. Thus, from the natural requirement on the interpolation $\boldsymbol{I}_G^L$, we see that

$$\boldsymbol{I}_G^L \boldsymbol{w}^G \equiv \boldsymbol{w}^L \equiv 1 \text{ on } \Gamma_{LG}. \tag{2.37}$$

By substituting (2.35), (2.36), and (2.37) into (2.21), we obtain

$$\int_{\Omega^L} \nabla \left(1 - \sum_{i \in \Gamma_P^L} N_i^L\right) \cdot \boldsymbol{\sigma} \nabla \phi^L d\Omega + \int_{\overline{\Omega_L^G}} \nabla \left(1 - \sum_{j \in \Gamma_P^G} N_j^G\right) \cdot \boldsymbol{\sigma} \nabla \phi^G d\Omega$$
$$+ \int_{\Omega_H^L} \nabla \left(1 - \sum_{i \in \Gamma_P^L} N_i^L\right) \cdot \boldsymbol{\sigma}_{\mathrm{i}} \nabla V_{\mathrm{m}}^L d\Omega = 0.$$

By expanding the above equation, we obtain (2.34). ∎

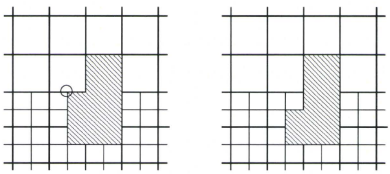

Fig. 2.5 *An undesired example for conservation* (a) *and the correction making this example conservative* (b). *In* (a), *a hanging node (marked with a circle) is located at the corner of the electrode.*

Physically, the residual at the electrode boundaries Γ_P can be interpreted as the current entering the torso through the surface of the electrodes. Here we assume that the weak solution ϕ to (2.16) is also the strong solution around Γ_p under a certain regularity of $\boldsymbol{\sigma}_\mathrm{e}$. That is, if the strong form equation

$$-\nabla \cdot \boldsymbol{\sigma}_\mathrm{e} \nabla \phi = 0 \text{ around } \Gamma_P \tag{2.38}$$

holds, we obtain from the Gauss divergence theorem

$$-\int_{\Omega^L} \nabla N_i^L \cdot \boldsymbol{\sigma}_\mathrm{e} \nabla \phi d\Omega = -\int_{\Gamma_P^L} N_i^L \vec{n} \cdot \boldsymbol{\sigma}_\mathrm{e} \nabla \phi d\Gamma, \ i \in \Gamma_P^L, \tag{2.39}$$

$$-\int_{\Omega^G} \nabla N_j^G \cdot \boldsymbol{\sigma}_\mathrm{e} \nabla \phi d\Omega = -\int_{\Gamma_P^G} N_j^G \vec{n} \cdot \boldsymbol{\sigma}_\mathrm{e} \nabla \phi d\Gamma, \ j \in \Gamma_P^G. \tag{2.40}$$

Here, $\vec{n}$ is the normal outward unit vector at Γ_P. Note that we assume that the electrode boundaries Γ_P are not attached to the heart muscle Ω_H. Thus, V_m and $\boldsymbol{\sigma}_\mathrm{i}$ do not appear in the equations. If we replace the analytical solutions on the left-hand sides of (2.39) and (2.40) by their discrete finite element approximations, they are, in fact, the residual components. Thus, the residual components $r_i^L, i \in \Gamma_P^L$, and $r_j^G, j \in \Gamma_P^G$, are the approximations of the fluxes on the right-hand sides of (2.39) and (2.40), respectively. If the interaction with the electric circuit connected to the electrodes is taken into account, the summations of the residual components at the electrode surfaces can be identified with the currents from the electrodes.

So far we have assumed that the electrode surface Γ_P does not intersect the interface boundary Γ_{LG}. However, this restriction is not essential for conservation, which is ensured as long as the boundaries Γ_{LG} follow the edges of the coarser elements at any interface. Figure 2.5 depicts an undesired example for conservation (a) and the correction making this example conservative (b). Note that a hanging node (marked with a circle) is located at the corner of the electrode in the undesired example. In general, we modify the definition of the test function w^L in (2.35) to match w^G in (2.36) at the interface:

$$w^L = 1 - \sum_{i \in \Gamma_P \setminus \Gamma_{LG}} N_i^L - \sum_{j \in \Gamma_P \cap \Gamma_{LG}} \boldsymbol{N}^L \left(\boldsymbol{I}_G^L \boldsymbol{\delta}_j^G \right)_{\Gamma_{LG}}. \tag{2.41}$$

Here, $\boldsymbol{\delta}_j^G$ is the vector on $\overline{\Omega_L^G}$ set to 1 at j and zero at the other nodes. From the above definition, we see that $\boldsymbol{I}_G^L \boldsymbol{w}^G \equiv \boldsymbol{w}^L$ holds at Γ_{LG}. By substituting this test

function into (2.21), we once again obtain (2.34) with the following definition of the residual at the interface:

$$r_j = -(\overline{\boldsymbol{K}_L^G}\boldsymbol{\phi}^G)_j - \left(\boldsymbol{I}_G^{L^T}(\boldsymbol{K}^L\boldsymbol{\phi}^L + \boldsymbol{K}_{\mathrm{i}}^L\boldsymbol{V}_{\mathrm{m}}^L)\right)_j, \quad j \in \Gamma_{LG} \cap \Gamma_P. \tag{2.42}$$

Thus, in computing the residual component at the interface, the contributions from the residual components on the neighboring fine mesh hanging nodes must be taken into account.

3. The Local-Global Multigrid Algorithm on a Composite Mesh.

3.1. Derivation of the Algorithm. Let us define the matrices $\boldsymbol{K}_L^G$ and $\boldsymbol{K}^G$ on the global mesh by

$$\boldsymbol{K}_L^G = \sum_{e^G \in E_L^G} \boldsymbol{K}^G(e^G), \tag{3.1}$$

$$\boldsymbol{K}^G = \sum_{e^G \in E^G} \boldsymbol{K}^G(e^G). \tag{3.2}$$

From the above definitions and (2.25), $\boldsymbol{K}^G$ is obtained by superposing $\boldsymbol{K}_L^G$ and $\overline{\boldsymbol{K}_L^G}$. Thus,

$$\boldsymbol{K}^G = \boldsymbol{K}_L^G + \overline{\boldsymbol{K}_L^G}. \tag{3.3}$$

Based on an idea proposed by Brandt [2], we add $\boldsymbol{K}_L^G\boldsymbol{\phi}^G$ to both sides of (2.30). Then we obtain the following equations equivalent to (2.29) and (2.30):

$$\boldsymbol{K}^L\boldsymbol{\phi}^L = -\boldsymbol{K}_{\mathrm{i}}^L\boldsymbol{V}_{\mathrm{m}}^L \text{ on } \Omega^L \backslash (\Gamma_{LG} \cup \Gamma_P), \tag{3.4}$$

$$\boldsymbol{\lambda} = -\boldsymbol{K}^L\boldsymbol{\phi}^L - \boldsymbol{K}_{\mathrm{i}}^L\boldsymbol{V}_{\mathrm{m}}^L \text{ on } \Gamma_{LG}, \tag{3.5}$$

$$\boldsymbol{K}^G\boldsymbol{\phi}^G = \boldsymbol{I}_G^{L^T}\boldsymbol{\lambda} + \boldsymbol{K}_L^G\boldsymbol{\phi}^G \text{ on } \Omega^G \backslash \Gamma_P. \tag{3.6}$$

If we define the residual vector $\boldsymbol{r}^L$ on the local mesh from (3.4), not only on $\Omega^L \backslash (\Gamma_{LG} \cup \Gamma_P)$ but also on Γ_{LG}, by

$$\boldsymbol{r}^L = -\boldsymbol{K}_{\mathrm{i}}^L\boldsymbol{V}_{\mathrm{m}}^L - \boldsymbol{K}^L\boldsymbol{\phi}^L \text{ on } \Omega^L \backslash \Gamma_P, \tag{3.7}$$

we see that it is identical to the Lagrange multiplier on Γ_{LG} from (3.5),

$$\boldsymbol{\lambda} = \boldsymbol{r}^L \text{ on } \Gamma_{LG}. \tag{3.8}$$

The above consideration naturally leads to the local-global solution process, shown in Figure 3.1, where steps (1) and (2) are iterated. Here, the injection $\boldsymbol{I}_L^G$ is performed by injecting the local mesh nodal values into the global mesh nodes on Ω_L^G. Note that the correction with the interpolation is also performed on the interface Γ_{LG} in the global mesh correction phase. Thus, together with the assumption on the initial guess, the constraint condition in (2.20) is always satisfied. As for the relaxation on the local and global meshes, a multigrid V-cycle can be applied. In particular, for the local mesh relaxation, one V-cycle is sufficient to smooth the error with respect to the global mesh resolution, where the coarsest mesh of the V-cycle on the local mesh has the same spatial resolution as the global mesh in our implementation, as depicted in Figure 3.2.

The local-global multigrid algorithm.
(0) Start
- $\boldsymbol{g}^L := -\boldsymbol{K}_{\mathrm{i}}^L \boldsymbol{V}_{\mathrm{m}}^L$
- Prepare an initial guess $\{\boldsymbol{\phi}^L, \boldsymbol{\phi}^G\}$ such that $\boldsymbol{\phi}^L = \boldsymbol{I}_G^L \boldsymbol{\phi}^G$ on Γ_{LG}

(1) Global mesh correction
- Compute the residual on the local mesh $\boldsymbol{r}^L := \mathbf{g}^L - \boldsymbol{K}^L \boldsymbol{\phi}^L$ on $\Omega^L \backslash \Gamma_P$
- Inject the local mesh solution $\boldsymbol{\phi}^G := \hat{\boldsymbol{I}}_L^G \boldsymbol{\phi}^L$ on Ω_{i}^G
- Store $\boldsymbol{\phi}^G$ in another vector $\hat{\boldsymbol{\phi}}^G := \boldsymbol{\phi}^G$
- Compute the right-hand side $\mathbf{g}^G := \boldsymbol{K}_{\mathrm{i}}^G \hat{\boldsymbol{\phi}}^G + \boldsymbol{I}_G^{L^T} \boldsymbol{r}^L$
- Compute an approximation for $\boldsymbol{K}^G \boldsymbol{\phi}^G = \mathbf{g}^G$ with the fixed boundary values on Γ_P
- Correction with the interpolation $\boldsymbol{\phi}^L := \boldsymbol{\phi}^L + \boldsymbol{I}_G^L (\boldsymbol{\phi}^G - \hat{\boldsymbol{\phi}}^G)$ on Ω^L

(2) Smoothing on the local mesh
- Relax the interior components of $\boldsymbol{\phi}^L$ for $\boldsymbol{K}^L \boldsymbol{\phi}^L = \mathbf{g}^L$ with the fixed boundary values on $\Gamma_{LG} \cup \Gamma_P$

Fig. 3.1 *The local-global multigrid algorithm.*

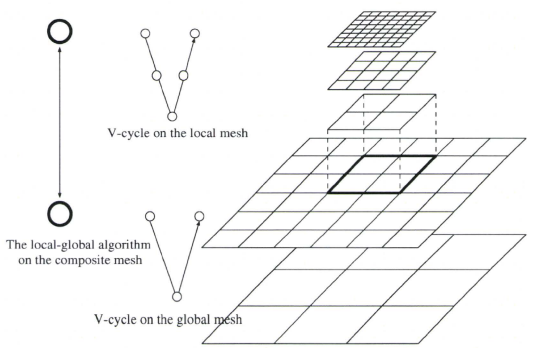

Fig. 3.2 *A sketch of the local-global multigrid algorithm. In each mesh, the multigrid V-cycle is applied as a smoother. In particular, the coarsest grid of the local mesh V-cycle has the same resolution as the finest global mesh.*

The local-global multigrid algorithm obtained above is similar to the multilevel adaptive technique (MLAT) proposed by Brandt [2]. However, the MLAT was described for finite difference or finite volume discretizations [22] and derived from the full approximation scheme (FAS) [2, 22], originally proposed to solve a nonlinear problem with a multigrid. An interesting point here is that the MLAT is naturally derived by extending the Lagrange multiplier in (3.6) at the local-global interface Γ_{LG} to the inside of the fine finite element mesh, where it can be interpreted as the residual. Also note that in the standard implementation of MLAT [22], the residual at the fine

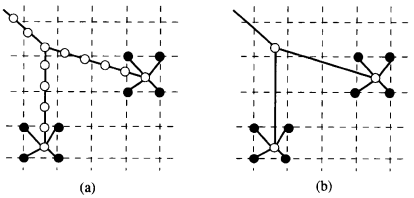

Fig. 3.3 *Original Purkinje network* (a) *and the network after the elimination* (b). *Black nodes are shared nodes with the voxel mesh.*

grid boundary is not transferred to the coarse grid, whereas in the above algorithm the residual components at the local mesh interface boundaries certainly affect the right-hand side of the coarse mesh equation. As we have seen in section 2.3, this is an essential point to ensure the conservation property at the local-global interface. Other techniques to ensure conservation have been introduced, for example, in [1, 14, 31] for finite volume discretizations. On the other hand, in common adaptive finite element approaches, a special refinement strategy is adopted at the fine-coarse interface so that hanging nodes are not present. In these approaches, conservation is automatically ensured. However, a method that allows hanging nodes provides easier mesh generation, in particular, for hexahedral elements.

3.2. Treatment of the Purkinje Fiber Network. In this section, we describe the special treatment of the Purkinje fibers in the local-global multigrid algorithm. As mentioned in section 1, the Purkinje network is modeled by one-dimensional elements, as is commonly done in the cardiovascular literature. In our simulator, only end-point nodes of the Purkinje network are connected to the voxel mesh nodes, as shown in Figure 3.3(a). Although a fairly fine spatial resolution is required for the Purkinje one-dimensional elements, we can eliminate most of the unknowns before solving the potential problem. This situation is illustrated in Figure 3.3. Nodes on the Purkinje network with only two edges connected can be eliminated without increasing the number of edges. Therefore, we do not apply any coarsening to the matrix on the reduced Purkinje nodes when constructing the matrix at the coarse level. In this case, although we have to invert the matrix completely on the reduced Purkinje nodes at the smoothing steps at each level of the multigrid cycle, this does not result in a crucial overhead due to the smaller size of the matrix on the reduced Purkinje nodes.

Here, we show how to construct the matrix on the global mesh for the reduced Purkinje network. In the following, the subscript letters "s" and "r" represent shared nodes and reduced Purkinje nodes, respectively. We assume that the shared nodes are included in the local voxel mesh nodes. Under this notation, a vector $\tilde{\phi}^L$ on the local mesh (involving the reduced Purkinje nodes) is represented as

$$\tilde{\phi}^L = \begin{bmatrix} \phi_{\mathrm{s}}^L \\ \phi_{\mathrm{r}}^L \end{bmatrix}. \tag{3.9}$$

According to the above block representation, the coefficient matrix on the local mesh

is then represented by

$$\tilde{\boldsymbol{K}}^L = \begin{bmatrix} \boldsymbol{K}^L + \boldsymbol{D}_{\mathrm{s}} & \boldsymbol{K}_{\mathrm{sr}} \\ \boldsymbol{K}_{\mathrm{rs}} & \boldsymbol{K}_{\mathrm{rr}} \end{bmatrix}. \tag{3.10}$$

Here, the matrices $\boldsymbol{D}_{\mathrm{s}}$, $\boldsymbol{K}_{\mathrm{sr}}$, $\boldsymbol{K}_{\mathrm{rs}}$, and $\boldsymbol{K}_{\mathrm{rr}}$ originate from the reduced stiffness matrices on the reduced Purkinje network. In order to construct an appropriate local-global multigrid algorithm, the reduced Purkinje network should also be connected to the global voxel mesh. In our approach, the matrix on the reduced Purkinje network is not coarsened, as mentioned above. Thus, the coefficient matrix on the global mesh is given by

$$\tilde{\boldsymbol{K}}^G = \begin{bmatrix} \boldsymbol{K}^G + \boldsymbol{I}_G^{L^T} \boldsymbol{D}_{\mathrm{s}} \boldsymbol{I}_G^L & \boldsymbol{I}_G^{L^T} \boldsymbol{K}_{\mathrm{sr}} \\ \boldsymbol{K}_{\mathrm{rs}} \boldsymbol{I}_G^L & \boldsymbol{K}_{\mathrm{rr}} \end{bmatrix}. \tag{3.11}$$

The interpolation $\tilde{\boldsymbol{I}}_G^L$ from the global to the local mesh involving the reduced Purkinje nodes is defined by

$$\tilde{\boldsymbol{I}}_G^L = \begin{bmatrix} \boldsymbol{I}_G^L & \boldsymbol{0} \\ \boldsymbol{0} & \boldsymbol{I} \end{bmatrix}. \tag{3.12}$$

Here, $\boldsymbol{I}$ denotes the identity mapping on the reduced Purkinje nodes. Under these matrices and mappings, the local-global multigrid algorithm in section 3.1 can also be performed with the Purkinje fiber network.

3.3. Relaxation of the Local-Global Multigrid Algorithm. In this section, we describe some details of the multigrid V-cycle that is applied "as the relaxation" in the local-global multigrid algorithm. As for the interpolation from the coarse to the fine mesh, we define two different operators, $\boldsymbol{I}_c^f$ and $\acute{\boldsymbol{I}}_c^f$, as follows. For $\boldsymbol{I}_c^f$, standard weights are chosen, whereby weights for the voxel mesh nodes that are outside Ω are set to zero. Note that the sum of the interpolation weights of $\boldsymbol{I}_c^f$ is not equal to one if one of the neighboring coarse nodes is outside Ω. In the definition of $\acute{\boldsymbol{I}}_c^f$, the weights are adjusted so that their sum is equal to one, except for the fine nodes, all of whose neighboring coarse nodes are outside Ω. In our implementation, we apply $\boldsymbol{I}_c^f$ as the interpolation operator and its transpose as the restriction operator in the multigrid V-cycles, whereas in the determination of the coefficient matrix $\boldsymbol{K}^c$ on the coarse mesh from the coefficient matrix $\boldsymbol{K}^f$ on the fine mesh, we apply $\acute{\boldsymbol{I}}_c^f$ as follows:

$$\boldsymbol{K}^c = (\acute{\boldsymbol{I}}_c^f)^T \boldsymbol{K}^f \acute{\boldsymbol{I}}_c^f. \tag{3.13}$$

In our experience, the above-mentioned strategy (using different interpolations in the multigrid cycle and in the determination of the coarse mesh matrix) results in the best convergence. For example, using $\acute{\boldsymbol{I}}_c^f$ for both stages leads to convergence stagnation when the Purkinje fiber network is connected, while using $\boldsymbol{I}_c^f$ for both stages results in slower convergence. Further study of this will be part of our future research.

The other key issue for robust convergence in the given potential problem is the choice of smoother in the multigrid. In this application, the electric conductivity has an anisotropy in the heart muscle along the fabric construction and also jumps in coefficients at the interfaces between different organs. Furthermore, the torso boundaries given on the finest level on the global mesh do not necessarily fit with the coarser voxel elements. These problems trigger convergence difficulties for the standard multigrid method. Therefore, we adopt an incomplete Cholesky (IC) smoother since it is

more powerful than a Gauss–Seidel smoother for jumping coefficient and anisotropic problems (see, for example, [22] or [33]). Thus, the coarse mesh correction may be somewhat less accurate. In the case where the Purkinje fiber network is connected, we apply the IC smoother on the voxel part and a sparse direct solution method on the reduced Purkinje network part with the two-block representation as in (3.10). In general, the linear equation to be solved at an arbitrary level can be represented as follows (see (3.11)):

$$\begin{bmatrix} \boldsymbol{K} + \boldsymbol{I}^{s\,T}\boldsymbol{D}_s\boldsymbol{I}^s & \boldsymbol{I}^{s\,T}\boldsymbol{K}_{sr} \\ \boldsymbol{K}_{rs}\boldsymbol{I}^s & \boldsymbol{K}_{rr} \end{bmatrix} \begin{bmatrix} \boldsymbol{\phi} \\ \boldsymbol{\phi}_r \end{bmatrix} = \begin{bmatrix} \boldsymbol{g} \\ \boldsymbol{g}_r \end{bmatrix}. \tag{3.14}$$

Here, $\boldsymbol{K}$ is the coefficient matrix on the grid where the smoother is applied, and $\boldsymbol{I}^s$ denotes the interpolation operator of the shared nodes on the finest local mesh Ω^L from the grid where the smoother is applied. Under the above notation, one smoothing step is described as follows:

$$\boldsymbol{r}^{(k)} = \boldsymbol{g} - (\boldsymbol{K} + \boldsymbol{I}^{s\,T}\boldsymbol{D}_s\boldsymbol{I}^s)\boldsymbol{\phi}^{(k)} - \boldsymbol{I}^{s\,T}\boldsymbol{K}_{sr}\boldsymbol{\phi}_r{}^{(k)}, \tag{3.15}$$

$$\text{Solve } \boldsymbol{M}\Delta\boldsymbol{\phi}^{(k+1)} = \boldsymbol{r}^{(k)}, \tag{3.16}$$

$$\boldsymbol{\phi}^{(k+1)} = \boldsymbol{\phi}^{(k)} + \Delta\boldsymbol{\phi}^{(k+1)}, \tag{3.17}$$

$$\boldsymbol{r}_r{}^{(k+1/2)} = \boldsymbol{g}_r - \boldsymbol{K}_{rr}\boldsymbol{\phi}_r^{(k)} - \boldsymbol{K}_{rs}\boldsymbol{I}^s\boldsymbol{\phi}^{(k+1)}, \tag{3.18}$$

$$\text{Solve } \boldsymbol{K}_{rr}\Delta\boldsymbol{\phi}_r^{(k+1)} = \boldsymbol{r}_r^{(k+1/2)}, \tag{3.19}$$

$$\boldsymbol{\phi}_r^{(k+1)} = \boldsymbol{\phi}_r^{(k)} + \Delta\boldsymbol{\phi}_r^{(k+1)}, \tag{3.20}$$

where $\boldsymbol{M}$ denotes the IC factorization of the matrix $\boldsymbol{K} + \boldsymbol{I}^{s\,T}\boldsymbol{D}_s\boldsymbol{I}^s$.

Another important technique to improve robustness is the Krylov subspace acceleration technique. One iteration of the multilevel solution is applied as a preconditioner for the Krylov subspace method. In the case of a composite mesh application, the implementation of a matrix-vector product may require considerable effort. However, as shown in the literature [3, 32], one can obtain a Krylov subspace acceleration by recombining iterants when their residuals are available. Details of our acceleration algorithm for this application are given in the literature [30].

4. Numerical Experiments with a Realistic Torso Model and Purkinje Fiber Network. In this section, we evaluate the performance of the local-global multigrid algorithm for a realistic model on which the real-life simulations described in section 1 are performed. In the model, the voxel mesh data of the organs in Figure 1.7 are prepared based on the Visible Human dataset [28]. The mesh sizes and intervals of the local and global voxel meshes are described in Table 4.1. The ratio of the local and global mesh intervals is equal to 4. An illustration of the Purkinje fiber network adopted in the simulation is depicted in Figure 4.1. The geometry of the network is based on an anatomical observation in [20]. Its conductivity is set to 100 mS/cm, which is much larger than the values in Table 1.1. The conductivity has been adjusted in order to reproduce the experimental observation of excitation propagation given in the literature [8]. The Purkinje-ventricular delay [15] is not taken into account in the current simulation, and the radius of the cross-section of the network is set to 0.05 cm except near the interconnection points with the heart muscle, where 0.01 cm or 0.03 cm is used. These radius values have also been adjusted in order to reproduce proper excitation conduction from the Purkinje fiber to the ventricular muscle. The total number of Purkinje nodes is 24509, of which 9882 nodes are shared with the local voxel mesh. The number of nonzero components in the matrix on the Purkinje

Table 4.1 *Local and global mesh sizes and intervals.*

Local mesh		Global mesh	
Size (x, y, z)	Interval length	Size (x, y, z)	Interval length
(288, 288, 368)	0.4 mm	(256, 256, 288)	1.6 mm

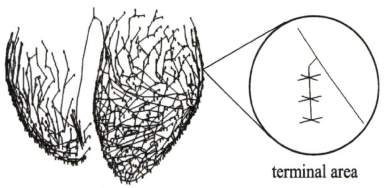

Fig. 4.1 *The Purkinje fiber network. At each terminal, the fiber is attached with* 12 *shared nodes.*

Table 4.2 *Elapsed time (in seconds) of one iteration of the local-global multigrid algorithm for the different divisions of the meshes.*

Division	L to G	G to L	Krylov	Smoother		Total
				Voxel	Purkinje	
$4 \times 4 \times 2$	0.09 (3.5%)	0.13 (4.9%)	0.12 (4.4%)	0.79 (30.1%)	0.30 (11.5%)	2.62
$4 \times 4 \times 3$	0.07 (3.4%)	0.09 (4.7%)	0.08 (4.4%)	0.56 (29.7%)	0.27 (14.4%)	1.89
$4 \times 4 \times 4$	0.05 (3.4%)	0.07 (4.7%)	0.06 (4.0%)	0.42 (27.8%)	0.22 (14.4%)	1.51
$4 \times 4 \times 5$	0.04 (3.3%)	0.06 (4.5%)	0.05 (3.9%)	0.33 (27.3%)	0.20 (16.1%)	1.22

network is 73709. However, after the reduction to the reduced Purkinje nodes, only 3937 nodes are left (besides the shared nodes). Finally, matrix $\boldsymbol{K}_{\mathrm{rr}}$ in (3.10) consists of 11989 nonzero components. The sparse LU factorization of matrix $\boldsymbol{K}_{\mathrm{rr}}$ has only 16481 nonzeros with a fill-in reduced ordering. Thus, the solution to $\boldsymbol{K}_{\mathrm{rr}}$ in (3.19) in the smoother is unlikely to produce a crucial overhead.

As for the relaxation on the local and global meshes, the multigrid V-cycle, with one pre- and one postsmoothing iteration, is applied. The V-cycle on the local mesh consists of three levels as the coarsest local mesh then has the same spatial resolution as the finest global mesh. One smoothing iteration is performed on the coarsest local mesh. The V-cycle on the global mesh consists of six levels. On the coarsest global mesh, twenty smoothing iterations are performed.

First, we examine the parallel performance of the local-global multigrid algorithm. Parallelization strategies used in our implementation are described in Appendix A. The timing results are measured on a PC-cluster composed of Pentium 4 processors (3.2GHz) connected via Myrinet. Shown in Table 4.2 are the elapsed times for the main processes in one iteration of the local-global multigrid algorithm, where the performance was examined for up to 80 processors. In the table, "L to G" and "G to L" denote the elapsed times for the local-to-global and global-to-local data transformations in (A.1), respectively. "Krylov" denotes the elapsed time for the Krylov acceleration. "Smoother" denotes the elapsed time for the smoothing iterations at

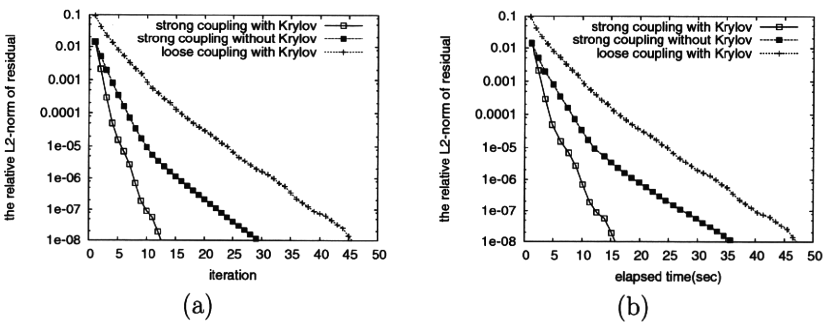

Fig. 4.2 *Convergence history with respect to* (a) *iterations and* (b) *elapsed time.*

all levels, where "Voxel" corresponds to the relaxation on the voxel meshes in (3.16) and (3.17), and "Purkinje" corresponds to the processes on the shared and reduced Purkinje nodes in (3.15), (3.18), (3.19), and (3.20). The numbers in parentheses are the ratios to the total time.

We observe a very satisfactory scaling. The elapsed times for the data transformations between the local and global meshes are relatively small in all cases. However, the elapsed time for the smoothing on the reduced Purkinje nodes is more pronounced as the number of processors increases. In particular, in (3.15) and (3.18), one-to-many communications are necessary to transfer the data to the shared nodes. It seems that this influences the parallel performance negatively.

Further, we analyze the convergence of the local-global multigrid algorithm. The convergence histories with respect to the number of iterations and the elapsed times are presented in Figure 4.2 for three different approaches. The notations "strong coupling with Krylov" and "strong coupling without Krylov" denote the local-global multigrid algorithm, respectively, with and without the Krylov acceleration technique, where the reduced Purkinje nodes are taken into account in the smoothing at every level, as described in section 3.3. On the other hand, the notation "loose coupling with Krylov" denotes the solution algorithm with the Krylov acceleration technique but solving the reduced Purkinje nodes and the voxel nodes in a decoupled way. This means that the direct solution on the reduced Purkinje nodes (including the shared nodes) and the local-global multigrid algorithm on the voxel mesh are performed alternately. In this case, the coupling with the reduced Purkinje nodes is dealt with only at the finest level on the local mesh.

In the Krylov acceleration technique, up to five iterants are recombined for the acceleration, and the acceleration process is restarted every five iterations. The results in Figure 4.2 show the effectiveness of the Krylov acceleration technique and the importance of the smoothing on the reduced Purkinje nodes at every level. The convergence speed of the loose coupling approach is obviously much slower than that of the proposed local-global multigrid algorithm. Even though there is considerable overhead in dealing with the reduced Purkinje nodes at every level, the proposed algorithm is still significantly faster than the loose coupling approach with respect to the elapsed time. In our real-life simulations, we commonly adopt 10^{-5} as the convergence tolerance for the relative L2-norm of the residual. Therefore, one solution takes approximately 8 seconds. If we solve the potential problem every 1 or 0.2 ms, about 8000 or 40000 seconds, respectively, are needed for the solutions to a 1 second

simulation with 80 processors. This is approximately 40 or 70%, respectively, of the total elapsed time in the ECG simulation to obtain the results given in Figure 2.2.

5. Conclusions. A parallel solution to the bidomain equation that appears in the excitation propagation analysis of the human heart was constructed. The stability of the explicit scheme was analyzed and an efficient multigrid technique to solve the potential problem with the torso model was introduced. In our approach, the potential problem was discretized on the composite mesh composed of a fine local mesh around the heart and a coarse global mesh covering the torso. A conservative finite element discretization adopting the Lagrange multiplier approach was introduced and a multigrid solution technique for this discretization was naturally derived. Furthermore, a method to combine the Purkinje fiber network with the multigrid solution technique was shown, whereby the matrix on the Purkinje network was reduced before entering the multilevel solver and the reduced matrix on the network was dealt with by a direct solution method at every level. The parallel efficiency and good convergence results were proved through an experiment with a realistic simulation model.

Appendix A. Parallelization Strategy. Here, we introduce the parallelization strategy of the bidomain analysis on a distributed memory parallel computer. Figure A.1 depicts the general situation for a composite mesh.

Note that there is no problem regarding the conservation discussed in section 2.3, even in the case where the local voxel mesh covers more than the torso region, as long as the boundaries of the torso on the local mesh coincide with the global mesh edges. In such a case, the local voxel mesh nodes on the torso boundaries are excluded from Γ_{LG}. Thus, there is no exchange of current there.

As shown on the right-hand side of Figure A.1, the solution process is decomposed into three phases with respect to data distribution between the processors. The first

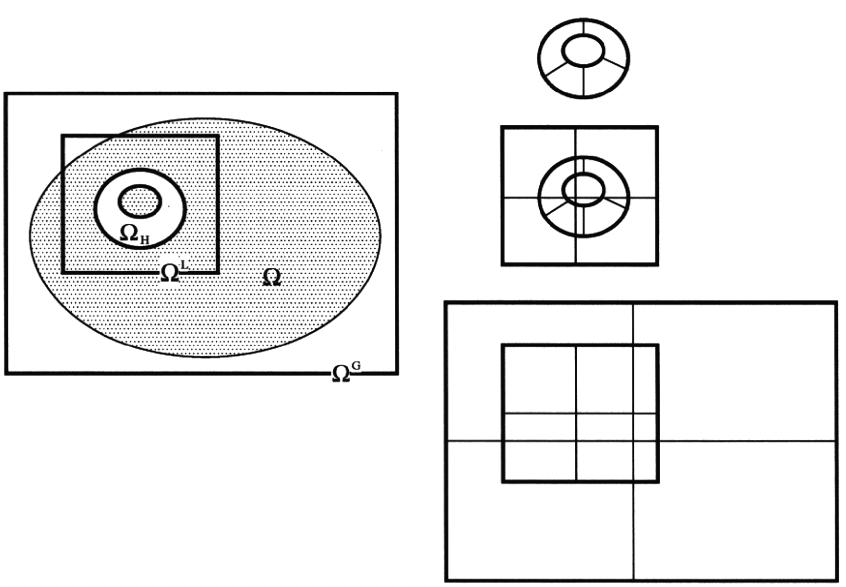

Fig. A.1 *(Left) two-dimensional image of three meshes (Ω_H (on the heart), Ω^L (local rectangular mesh), Ω^G (global rectangular mesh)) and (right) their partitioning (for 4 processes).*

phase corresponds to the explicit Euler time integration of the inner iteration described in section 2.1. Here, the computation is performed only at the nodes on the heart muscle Ω_H. The second and third phases include the local-global multigrid algorithm described in section 3.1 on the local and global voxel meshes, respectively. For the second and third phases, the nodes are partitioned regularly in each direction. In contrast, the first phase is based on a partitioning of an unstructured graph which consists only of the nodes on the heart muscle Ω_H. For the partitioning, we adopt the graph partitioning tool ParMETIS [10] to obtain the partitioning information. Since these data distributions are not consistent, as can be seen in Figure A.1, redistribution of variables takes place at each phase change. The variables that are redistributed at each phase change are described in the diagram below:

$$\begin{array}{ccc} & \Omega_H & \\ \boldsymbol{\phi}^L & \uparrow\downarrow & \boldsymbol{K}_{\mathrm{i}}\boldsymbol{V}_{\mathrm{m}} \\ & \Omega^L & \\ \boldsymbol{\phi}^G - \hat{\boldsymbol{\phi}}^G & \uparrow\downarrow & \boldsymbol{I}_G^{L\,T}\boldsymbol{r}^L, \hat{\boldsymbol{I}}_G^L\boldsymbol{\phi}^L. \\ & \Omega^G & \end{array} \tag{A.1}$$

The communication speed of the redistribution between the local and global meshes is crucial to the overall parallel performance because this redistribution is performed every cycle in the local-global multigrid algorithm. The overhead cost for the redistribution in the real-life application has been presented in section 4.

In each phase, parallelism is obtained in a standard way except for the IC smoother in the second and third phases. The IC smoother is modified, as it can easily be parallelized under the regular partitioning; that is, the local IC smoother is performed in each processor with one layer overlap at the subdomain boundaries.

In the case where the Purkinje fiber network is connected, the vectors $\boldsymbol{\phi}_{\mathrm{r}}$, $\boldsymbol{g}_{\mathrm{r}}$ and the matrices $\boldsymbol{K}_{\mathrm{sr}}$, $\boldsymbol{K}_{\mathrm{rs}}$, $\boldsymbol{K}_{\mathrm{rr}}$ in (3.14) are stored in one of the processors (say, Proc0), while the matrix for the interpolation on the shared nodes $\boldsymbol{I}^{\mathrm{s}}$ is distributed along the regular partitioning of the voxel mesh. Thus, the vector data $\boldsymbol{K}_{\mathrm{sr}}\boldsymbol{\phi}_{\mathrm{r}}^{(k)}$ on Proc0 is scattered in (3.15), and the distributed vector data $\boldsymbol{I}^{\mathrm{s}}\boldsymbol{\phi}^{(k+1)}$ is gathered to Proc0 in (3.18). This process may generate considerable overhead when the number of shared nodes is large.

Acknowledgments. The authors would like to thank S. Sugiura (University of Tokyo, M.D.), K. Sunagawa (Kyushu University Faculty of Medicine, M.D.), and M. Sugimachi and M. Inagaki (National Cardiovascular Center Research Institute, M.D.) for their support in constructing the heart muscle and torso models and for their useful suggestions in improving the accuracy of the simulation. They would like to thank H. Koga for his great contribution in constructing the Purkinje fiber network model. Finally, they would also like to thank C. W. Oosterlee, Ph.D., for reading the manuscript and for the useful comments.

REFERENCES

[1] D. Bai and A. Brandt, *Local mesh refinement multilevel techniques*, SIAM J. Sci. Statist. Comput., 8 (1987), pp. 109–134.

[2] A. Brandt, *Multi-level adaptive solutions to boundary-value problems*, Math. Comp., 31 (1977), pp. 333–390.

[3] A. Brandt and V. Mikulinsky, *On recombining iterants in multigrid algorithms and problems with small islands*, SIAM J. Sci. Comput., 16 (1995), pp. 20–28.

[4] E. M. CHERRY, H. S. GREENSIDE, AND C. S. HENRIQUEZ, *Efficient simulation of three-dimensional anisotropic cardiac tissue using an adaptive mesh refinement method*, CHAOS, 13 (2003), pp. 853–865.
[5] S. CORTASSA, M. A. AON, B. O'ROURKE, R. JACQUES, H. J. TSENG, E. MARBAN, AND R. L. WINSLOW, *A computational model integrating electrophysiology, contraction, and mitochondrial bioenergetics in the ventricular myocyte*, Biophys. J., 91 (2006), pp. 1564–1589.
[6] M. COURTEMANCHE, R. J. RAMIREZ, AND S. NATTEL, *Ionic mechanisms underlying human atrial action potential properties: Insights from a mathematical model*, Amer. J. Physiol., 275 (2003), pp. H301–H321.
[7] D. DIFRANCESCO AND D. NOBLE, *A model of cardiac electrical activity incorporating ionic pumps and concentration changes*, Philos. Trans. R. Soc. Lond. Ser. B, 307 (1985), pp. 353–398.
[8] D. DURRER, R. TH. VAN DAM, G. E. FREUD, M. J. JANSE, F. L. MEIJLER, AND R. C. ARZBAECHER, *Total excitation of the isolated human heart*, Circulation, 41 (1970), pp. 899–912.
[9] D. A. HOOKS, K. A. TOMLINSON, S. G. MARSDEN, I. J. LEGRICE, B. H. SMAILL, A. J. PULLAN, AND P. J. HUNTER, *Cardiac microstructure: Implications for electrical propagation and defibrillation in the heart*, Circ. Res., 91 (2002), pp. 331–338.
[10] G. KARYPIS, K. SCHLOEGEL, AND V. KUMAR, *ParMETIS*, http://www-users.cs.umn.edu/karypis/metis/parmetis/.
[11] P. KOHL, K. DAY, AND D. NOBLE, *Cellular mechanisms of cardiac mechano-electric feedback in a mathematical model*, Can. J. Cardiol., 14 (1998), pp. 111–119.
[12] M. W. KROLL AND M. H. LEHMANN, *Implantable Cardioverter Defibrillator Therapy*, Kluwer Academic, Norwell, MA, 1996.
[13] CH. LUO AND Y. RUDY, *A model of the ventricular cardiac action potential. Depolarization, repolarization, and their interaction*, Circ. Res., 68 (1991), pp. 1501–1526.
[14] S. F. MCCORMICK, *Multilevel Adaptive Methods for Partial Differential Equations*, Frontiers Appl. Math. 6, SIAM, Philadelphia, 1989.
[15] C. MENDEZ, W. J. MUELLER, AND X. URGUIAGA, *Propagation of impulses across the Purkinje fiber-muscle junctions in the dog heart*, Circ. Res., 26 (1970), pp. 135–150.
[16] M. PENNACCHIO, *The mortar finite element method for the cardiac bidomain model of extracellular potential*, J. Sci. Comput., 20 (2004), pp. 191–210.
[17] G. PLANK, M. LIEBMANN, R. WEBER DOS SANTOS, E. J. VIGMOND, AND G. HASSE, *Algebraic multigrid preconditioner for the cardiac bidomain model*, IEEE Trans. Biomed. Engrg., 54 (2007), pp. 585–596.
[18] R. PLONSEY, *Bioelectric sources arising in excitable fibers (ALZA lectures)*, Ann. Biomed. Engrg., 16 (1988), pp. 519–546.
[19] J. SUNDNES, G. T. LINES, K. A. MARDAL, AND A. TVEITO, *Multigrid block preconditioning for a coupled system of partial differential equations modeling the electrical activity in the heart*, Comput. Methods Biomech. Biomed. Engrg., 5 (2002), pp. 397–409.
[20] S. TAWARA, *Das Reitzleitungssystem des Saugetierherzens: Eine anatomisch-histologische Studie über das Atrioventrikularbundel und die Purkinjeschen Faden*, Gustav Fischer, Jena, Germany, 1906.
[21] K. H. W. J. TEN TUSSCHER, D. NOBLE, P. J. NOBLE, AND A. V. PANFILOV, *A model for human ventricular tissue*, Amer. J. Physiol. Heart Circ. Physiol., 286 (2004), pp. H1573–H1589.
[22] U. TROTTENBERG, C. OOSTERLEE, AND A. SCHÜLLER, *Multigrid*, Academic Press, San Diego, CA, 2001, pp. 356–381.
[23] L. TUNG, *A Bi-domain Model for Describing Ischemic Myocardial D-C Potentials*, Ph.D. Thesis, MIT, Cambridge, MA, 1978.
[24] *UT Heart Simulator*, http://www.sml.k.u-tokyo.ac.jp.
[25] E. J. VIGMOND AND C. CLEMENTS, *Construction of a computer model to investigate sawtooth effects in the Purkinje system*, IEEE Trans. Biomed. Engrg., 54 (2007), pp. 389–399.
[26] E. J. VIGMOND AND L. J. LEON, *Computationally efficient model for simulating electrical activity in cardiac tissue with fiber rotation*, Ann. Biomed. Engrg., 27 (1999), pp. 160–170.
[27] E. J. VIGMOND, F. AGUEL, AND N. A. TRAYANOVA, *Computational techniques for solving the bidomain equation*, IEEE Trans. Biomed. Engrg., 49 (2002), pp. 1260–1269.
[28] *The Visible Human Project*, http://www.nlm.nih.gov/research/visible/visible_human.html.
[29] R. WEBER DOS SANTOS, G. PLANK, S. BAUER, AND E. J. VIGMOND, *Parallel multigrid preconditioner for the cardiac bidomain model*, IEEE Trans. Biomed. Engrg., 51 (2004), pp. 1960–1968.
[30] T. WASHIO, J.-I. OKADA, AND T. HISADA, *A parallel multilevel technique for solving the bidomain equation on a human heart with Purkinje fibers and a torso model*, SIAM J. Sci. Comput., 30 (2008), pp. 2855–2881.

[31] T. WASHIO AND C. OOSTERLEE, *Error analysis for a potential problem on locally refined grids*, Numer. Math., 86 (2000), pp. 539–563.
[32] T. WASHIO AND C. OOSTERLEE, *Krylov subspace acceleration for nonlinear multigrid schemes*, Electron. Trans. Numer. Anal., 6 (1997), pp. 271–290.
[33] P. WESSELING, *Introduction to Multigrid Methods*, Wiley, Chichester, UK, 1992.
[34] H. WATANABE, S. SUGIURA, H. KAFUKU, AND T. HISADA, *Multiphysics simulation of left ventricular filling dynamics using fluid-structure interaction finite element method*, Biophys. J., 87 (2004), pp. 2074–2085.
[35] Q. ZHANG AND T. HISADA, *Analysis of fluid-structure interaction problems with structural buckling and large domain changes by ALE finite element method*, Comput. Methods Appl. Mech. Engrg., 190 (2001), pp. 6341–6357.

日本機械学会論文集(A編)
76巻772号(2010-12)

論文 No. 09-1046

力学・電気化学効果を考慮した心筋細胞モデル化に関する検討*

平林智子*1, 岡田純一*2, 鷲尾 巧*3
杉浦清了*3, 久田俊明*4

A Study on Mechano-Electrochemical Modeling of Cardiomyocyte

Satoko HIRABAYASHI*5, Jun-ichi OKADA, Takumi WASHIO,
Seiryo SUGIURA and Toshiaki HISADA

*5 Department of Mechanical Science and Engineering, Graduate School of Engineering, Nagoya University, Furo-cho, Chikusa-ku, Nagoya-shi, Aichi, 464-8603 Japan

Triphasic theory has been proposed to couple mechanical, chemical and electrical phenomena in the analysis of hydrated charged soft tissues. As a cardiac myocyte, which consists of a solid phase and a charged fluid phase filling its interstices, is this type of tissue, the applicability of the triphasic theory to the modeling of cardiac myocyte was discussed in this research. An efficient finite element formulation for large deformation analyses was newly developed. The concentration of each ion is set as a primary variable to treat major ions, such as sodium, calcium, and potassium, separately. Physiological features of cardiac myocyte, such as activities of ion channels and sarcoplasmic reliculum, were reasonably included into the new formulation. Even under a simple 2D modeling with limited number of parameters, the simulation qualitatively reproduced various cardiac behaviors such as excitations of cardiac cells induced by current stimuli and field stimuli.

Key Words: Biomechanics, Finite Element Method, Nonlinear Problem, Coupling Problem, Analytical Model, Triphasic Theory, Cardiac Myocyte, Cell Membrane, Ion Channel

1. 緒 言

心臓の活動の根元をなすのは心筋細胞における一連の生化学反応である．周囲の電位場の状況に応じて細胞膜のイオンチャネルを通じて各種イオンが出入りして脱分極を生じた結果，内部でカルシウムイオンの反応拡散現象が起こり，その濃度分布に応じて架橋運動による収縮力が発生する．この一連の活動は，電気(イオン電流，興奮伝播，心電図など)・化学(物質輸送，反応，エネルギー変換など)・力学(心筋張力，血圧，血流など)の諸現象に広く派生し，逆に電気(電位勾配)・化学(濃度勾配)・力学(移流)の全ての現象に影響される，マルチフィジックス問題である．2004年，酒谷らは．電位勾配とイオンの濃度勾配，電荷の保存則を全て連立して解くことで，神経細胞内外のイオン濃度と電位の時空間変化を同時に解析した[1]．2005年に岡田らは心筋細胞モデルの有限要素解析を行い，細胞内でのCa^{2+}の移動と，その濃度分布の変化による収縮力の発生と変形をシミュレートした[2]．今後は溶媒の流れも含めた電気化学・力学連成シミュレーションが研究課題の一つになってくると思われる．心筋細胞は複雑な構造の細胞組織の隙間をイオン電解質溶液である細胞内液が満たすような構造をとっている．このようなミクロ流動における電気化学・力学連成問題を取り扱うための理論として二相理論が提案されており，その非線形有限要素法への定式化が行われ，椎間板や軟骨といった生体の解析が試みられてきた[3]．しかし，その複雑さゆえ取り扱いが難しいこと，全てを連成して解くために計算量が膨大なことから応用例はまだ少ない．ここで，過去の心筋細胞の有限要素解析及び電気化学・力学連成有限要素解析について表1にまとめておく．

本研究では，力学・電気化学効果を考慮した心筋細胞モデルの作成への三相理論適用の可能性を検討することを目的とする．なお，後述のように心筋細胞の解析に際しては多くの種類のイオンを取り扱う必要があるため，三相理論の未知数の取り方を変更する事により低計算負荷に離散化する手法を考案し実装を行った．

2. 理 論

各イオンについて流速(3自由度)を未知数とする[3]と，取り扱うイオンの種類が多い場合には計算量が膨大になってしまう．混合体，流体，各イオンについて(電気)化学ポテンシャルを未知数として取り扱う手法

* 原稿受付 2009年11月20日．
*1 正員，名古屋大学大学院工学研究科機械理工学専攻(〒464-8603 名古屋市千種区不老町)．
*2 正員，東京大学大学院新領域創成科学研究科(〒277-8563 柏市柏の葉5-1-5)．
*3 東京大学大学院新領域創成科学研究科．
*4 正員，フェロー，東京大学大学院新領域創成科学研究科．
E-mail: hirabayashi@mech.nagoya-u.ac.jp

Table 1 Comparison of Related Studies

	Electrical Potential	Ion Concentration	Electroneutrality	Advection	Deformation	Membrane
Sakatani[1]	○	○	○	-	-	○
Okada[2]	-	○	-	-	○	○
Triphasic Theory[3]~[5]	○	○	○	○	○	-

Table 2 Primary Variables in the Proposed Method

	Number of Degrees of Freedom	*1	*2
Displacement of Solid	3	$\boldsymbol{u}^s$	$\boldsymbol{U}^s$
Relative Velocity of Fluid	3	$\boldsymbol{w}$	$\boldsymbol{W}$
Concentration of Ionα	1	c^α	C^α
Hydrostatic Pressure	1	p	P
Electrostatic Potential	1	ψ	Ψ

*1 Current Configuration
*2 Imaginary Reference Configuration

も存在する[4]が，この方法では未知数は減っても連成の定式化が複雑になってしまうため，収束が遅くなって結果的に計算量が増えてしまう可能性がある．そこで本研究では表2に示すような量を未知数とすることにして定式化をしなおす．これにより，計算量を減らして複数種類のイオンを別々に取り扱うこと，ひいてはイオンチャネルや筋小胞体といった心筋細胞の生理学的特徴を定式化の中に論理的に組み込むことが可能となった．c^α は単位流体体積におけるモル濃度を表す．

2·1 支配方程式の導出 混合体理論 (Mixture Theory) に基づく三相理論[5]では混合体を構成する要素である固体相（空孔をもつスケルトン），流体相，イオン相が巨視的に同じ空間位置を同時に占有すると仮定する．変形に伴いそれぞれの相は分離していくため，過去の例[3]にならい，変形前の固体相を全ての相における参照配置 χ とする．

現配置と参照配置における微分演算子をそれぞれ ∇, ∇_χ，変形勾配を $\boldsymbol{F}$ とすると任意のベクトルまたはテンソル $\boldsymbol{a}$，及び任意のスカラー b を $\boldsymbol{F}$ の行列式 J を用いた Piola 変換して得られた値 $\boldsymbol{A} \equiv J\boldsymbol{F}^{-1}\cdot\boldsymbol{a}, B \equiv b$ に対して次式が成立する[3]．

$$\nabla_\chi \cdot \boldsymbol{A} = J\nabla\cdot\boldsymbol{a} \tag{1}$$

$$\nabla_\chi B = \boldsymbol{F}^T\nabla b \tag{2}$$

わかりやすくするために，$B \equiv b$ のように Piola 変換後も不変な値も違う表記を用いた．

流体相の粘性を無視すると，混合体全体のコーシー応力 $\boldsymbol{\sigma}$ は，不定静水圧 p と混合体中の固体相の変形により生じる応力成分 $\boldsymbol{\sigma}^e$ の合計となる[3]．

$$\boldsymbol{\sigma} = -p\boldsymbol{I} + \boldsymbol{\sigma}^e \tag{3}$$

単位体積あたりの水分の化学ポテンシャル μ^w 及び各イオン α の 1mol あたりの電気化学ポテンシャル $\tilde{\mu}^\alpha$ は次式により与えられる[3]．

$$\mu^w = \mu_0^w + (p - RT\phi c^{total}) \tag{4}$$

$$\tilde{\mu}^\alpha = \mu_0^\alpha + RT\ln(\gamma^\alpha c^\alpha) + z^\alpha\psi \tag{5}$$

μ_0^w 及び μ_0^α はそれぞれ水分，イオン α の基準化学ポテンシャル；R は気体定数；T は絶対温度；ϕ は浸透係数 (osmotic coefficient)；c^{total} は単位流体体積におけるイオンモル濃度の合計つまり $\sum_\alpha c^\alpha$；γ^α は α の活性係数 (c^α が十分薄いので以下の議論では理想値 1 であるとする)；z^α は α の価数；である．

また，固体相に対する流体の相対速度，イオン α の相対モル流束をそれぞれ以下のように定義しておく[3]．

$$\boldsymbol{w} = \phi^w(\boldsymbol{v}^w - \boldsymbol{v}^s) \tag{6}$$

$$\boldsymbol{j}^\alpha = c^\alpha\phi^w(\boldsymbol{v}^\alpha - \boldsymbol{v}^s) \tag{7}$$

ここで，$\boldsymbol{v}^s$, $\boldsymbol{v}^w$, $\boldsymbol{v}^\alpha$ はそれぞれ固体，流体，各イオン α の Euler 座標系における速度；ϕ^w は流体の含有率である．また，$\boldsymbol{w}$, $\boldsymbol{j}^\alpha$ を Piola 変換したものをそれぞれ $\boldsymbol{W}$, $\boldsymbol{J}^\alpha$ と表記する．

2·1·1 電気的中性条件 電気的中性条件は次のような式で表され，全ての点で満たされるとする[3]．

$$\sum_\alpha (z^\alpha c^\alpha) + c^F = 0 \tag{8}$$

ここで c^F は単位流体体積あたりの固定電荷 (固体に束縛されて動けない電荷) である．電気的中性条件式の時間微分は以下のようになる．

$$\left(\sum_\alpha (z^\alpha c^\alpha) + c^F\right)^{\cdot} = \sum_\alpha (z^\alpha \dot{C}^\alpha) + \dot{C}^F = 0 \tag{9}$$

任意の値 $\mathscr{A}$ に対して $\dot{\mathscr{A}}$ は次のように定義した．

$$\dot{\mathscr{A}} \equiv \left.\frac{\partial \mathscr{A}}{\partial t}\right|_\chi \tag{10}$$

2·1·2 平衡方程式 本論文では細胞レベルの微小なスケールの問題を取り扱うため，慣性力は無視する．

$\boldsymbol{\sigma}$ を Piola 変換したものを $\boldsymbol{\Pi}$ とすると参照配置での混合体の平衡方程式は次式となる[3]．

$$\nabla_\chi \cdot \boldsymbol{\Pi} = \boldsymbol{0} \tag{11}$$

固体・イオン間の摩擦力は無視できるとすると，単位体積あたりの混合体内で電解質溶液が受ける摩擦力 $\boldsymbol{\pi}_{ws}$ は溶媒が固体から受ける摩擦力のみになる．この値は溶媒の含有率 ϕ^w の二乗に比例することが知られている[6]ので，式(6)を用いて次のように表すことができる．$\boldsymbol{\kappa}$ は混合体における流体の透過度(浸透係数)を表す．

$$\boldsymbol{\pi}_{ws} = (\phi^w)^2 \boldsymbol{\kappa}^{-1} \cdot (\boldsymbol{v}^w - \boldsymbol{v}^s) = \phi^w \boldsymbol{\kappa}^{-1} \cdot \boldsymbol{w} \tag{12}$$

定常状態では次の平衡方程式が成り立つ．

$$\phi^w \nabla \mu^w + \sum_\alpha (c^\alpha \phi^w \nabla \tilde{\mu}^\alpha) + \boldsymbol{\pi}_{ws} = 0 \tag{13}$$

式(4)，(5)，(12)を代入し，さらに電気的中性条件の式(8)を用いて整理すると次式が得られる．

$$\nabla p + RT(1-\phi)\nabla c^{total} + \boldsymbol{\kappa}^{-1} \cdot \boldsymbol{w} - c^F \nabla \psi = 0 \tag{14}$$

左辺第二項はイオンの薄いほうから濃いほうに溶媒が流れる力であり，一般に浸透圧と呼ばれ浸透係数 ϕ によって強さが変わる．$\boldsymbol{F}^T$ をかけてPiola変換すると次の式が得られる．

$$\nabla_\chi P + RT(1-\phi)\nabla_\chi C^{total} + \boldsymbol{K}^{-1} \cdot \boldsymbol{W} - C^F \nabla_\chi \Psi = 0 \tag{15}$$

$$\boldsymbol{K}^{-1} \equiv \frac{1}{J} \boldsymbol{F}^T \cdot \boldsymbol{\kappa}^{-1} \cdot \boldsymbol{F} \tag{16}$$

イオンにかかる力は，電気化学ポテンシャルの勾配と流体から受ける摩擦力である．固体，及び他のイオンとの摩擦力は十分小さいので無視できるとする．流体との摩擦力は，流体の含有率 ϕ^w 及び絶対温度に比例し，イオンと流体の相対速度の方向に働き，異方性はなく，変形によって変化しないとすると，定常状態では各イオン α に関して次の平衡方程式が成り立つ．

$$\begin{aligned} &\nabla \tilde{\mu}^\alpha + \frac{\phi^w RT}{d^\alpha}(\boldsymbol{v}^\alpha - \boldsymbol{v}^w) \\ &= \frac{RT}{c^\alpha}\nabla c^\alpha + z^\alpha \nabla \psi + \frac{RT}{c^\alpha d^\alpha}(\boldsymbol{j}^\alpha - c^\alpha \boldsymbol{w}) = 0 \end{aligned} \tag{17}$$

定数 d^α はイオンの拡散率を表す．この式を変形すると

$$\boldsymbol{j}^\alpha = c^\alpha \boldsymbol{w} - d^\alpha \left(\nabla c^\alpha + \frac{c^\alpha}{RT} z^\alpha \nabla \psi \right) \tag{18}$$

となり，Piola変換すると次の式が得られる．

$$\boldsymbol{J}^\alpha = C^\alpha \boldsymbol{W} - \boldsymbol{D}^\alpha \cdot \left(\nabla_\chi C^\alpha + \frac{z^\alpha}{RT} C^\alpha \nabla_\chi \Psi \right) \tag{19}$$

$$\boldsymbol{D}^\alpha = J d^\alpha \boldsymbol{F}^{-1} \cdot \boldsymbol{F}^{-T} = J d^\alpha \boldsymbol{C}^{-1} \tag{20}$$

式(18, 19)右辺は順番に移流，濃度勾配，電位勾配による流れを表している．

2·1·3 連続の式　流体に関して，物質点の参照座標に対する速度を $\tilde{\boldsymbol{v}}^w$ とすると，Euler座標系に対する物質点及び参照座標系の速度 $\boldsymbol{v}^w$，$\boldsymbol{v}^s$ との関係は次のように表せる[7]．

$$\tilde{\boldsymbol{v}}^w = \boldsymbol{F}^{-1} \cdot (\boldsymbol{v}^w - \boldsymbol{v}^s) = \frac{1}{\phi^w} \boldsymbol{F}^{-1} \cdot \boldsymbol{w} = \frac{1}{J\phi^w} \boldsymbol{W} \tag{21}$$

また，流体の本当の密度を ρ_T^w とおくと参照座標系における流体の質量密度は $J\phi^w \rho_T^w$ と表せるので，参照座標系の表記による連続の式[7]は下記のように表される．

$$(J\phi^w \rho_T^w)^{\cdot} + \nabla_\chi \cdot (J\phi^w \rho_T^w \tilde{\boldsymbol{v}}^w) = 0 \tag{22}$$

これらの式及び流体が非圧縮 $(\dot{\rho}_T^w = 0)$ で一様である $(\nabla_\chi \rho_T^w = 0)$ という仮定から次の式が得られる．

$$(J\phi^w)^{\cdot} + \nabla_\chi \cdot \boldsymbol{W} \equiv \dot{\Phi}^w + \nabla_\chi \cdot \boldsymbol{W} = 0 \tag{23}$$

参照座標系におけるイオンの質量密度は原子量を M^α として $\phi^w c^\alpha M^\alpha$ と表せることから，イオンに関しても同様にして次の式が得られる．

$$(JC^\alpha \phi^w)^{\cdot} + \nabla_\chi \cdot \boldsymbol{J}^\alpha = \dot{C}^\alpha \Phi^w + \dot{\Phi}^w C^\alpha + \nabla_\chi \cdot \boldsymbol{J}^\alpha = 0 \tag{24}$$

式(23)，(24)より次の式が得られる．

$$\dot{C}^\alpha \Phi^w - C^\alpha \nabla_\chi \cdot \boldsymbol{W} + \nabla_\chi \cdot \boldsymbol{J}^\alpha = 0 \tag{25}$$

2·1·4 非圧縮の条件式　$\dot{\boldsymbol{Q}}^w = \boldsymbol{W}$ とする参照配置における流体相の積算流出量ベクトル $\boldsymbol{Q}^w$(初期値0)を定義すると，参照配置におけるイオン相体積を無視した三相構造の非圧縮条件は次のようになる[3]．

$$J - 1 + \nabla_\chi \cdot \boldsymbol{Q}^w = 0 \tag{26}$$

2·2 弱形式化　前節で得られた式(11)，(15)に対して重み関数 $\delta \boldsymbol{U}^s$ 及び $\delta \boldsymbol{Q}^w$ を用いて弱形式化し，同時にLagrange乗数 λ^α，λ^p，λ^Ψ を用いてそれぞれ付帯条件(25)，(26)，(9)を導入する．参照配置における固体相の体積領域 Ω 及び表面領域 Γ_t，Γ_w 及び Γ_α について積分し，さらに $\delta \boldsymbol{u}^s$，$\delta \boldsymbol{Q}^w$，$\delta \lambda^\alpha$ をそれぞれ可容変位場，可容流体相積算流出量場，可容イオン濃度場として発散定理を適用して，式(19)を代入すると次の式が得られる．

$$\begin{aligned} &\int_\Omega [\boldsymbol{S} : \delta \boldsymbol{E} + (\nabla_\chi \cdot \delta \boldsymbol{Q}^w)\left(P + RT(1-\phi)C^{total} + C^F \Psi\right) \\ &\quad - \delta \boldsymbol{Q}^w \cdot (\boldsymbol{K}^{-1} \cdot \boldsymbol{W}) + (\dot{C}^\alpha \Phi^w + \boldsymbol{W} \cdot \nabla_\chi C^\alpha)\delta \lambda^\alpha \\ &\quad + \nabla_\chi \delta \lambda^\alpha \cdot \boldsymbol{D}^\alpha \cdot \left(\nabla_\chi C^\alpha + \frac{z^\alpha}{RT} C^\alpha \nabla_\chi \Psi \right) \\ &\quad + (1 - J - \nabla_\chi \cdot \boldsymbol{Q}^w)\delta \lambda^p + \left\{ \sum_\alpha (z^\alpha \dot{C}^\alpha) + \dot{C}^F \right\} \delta \lambda^\Psi] dV \\ &- \int_{\Gamma_t} \delta \boldsymbol{U}^s \cdot \bar{\boldsymbol{T}} dS - \int_{\Gamma_w} (\bar{C}^F \bar{\Psi} + RT(1-\phi)\bar{C}^{total} + \bar{P}) \boldsymbol{n} \cdot \delta \boldsymbol{Q}^w dS \\ &- \int_{\Gamma_\alpha} \delta \lambda^\alpha (\bar{C}^\alpha \bar{\boldsymbol{W}} - \bar{\boldsymbol{J}}^\alpha) \cdot \boldsymbol{n} dS = 0 \end{aligned} \tag{27}$$

$$\boldsymbol{S} \equiv \boldsymbol{\Pi} \cdot \boldsymbol{F}^{-T} = \boldsymbol{S}_E^S - PJ\boldsymbol{C}^{-1} \tag{28}$$

$\bar{}$は境界で与えられる物理量を表し，$\bar{\boldsymbol{T}}$は公称応力ベクトルである．$\boldsymbol{S}$及び$\boldsymbol{S}_E^S$は混合体及び固体相における変形による第2 Piola-Kirchhoff応力であり，$\boldsymbol{S}_E^S$は空孔率も反映した巨視的な弾性ポテンシャル関数Wにより次式のように与えられるものとする．

$$\boldsymbol{S}_E^S = 2\partial W / \partial \boldsymbol{C} \tag{29}$$

2·3 離散化　表2に示すような値を未知数として式(27)を有限要素離散化すると下記のような非線型方程式が得られる．

$$\boldsymbol{F}_{int} = \boldsymbol{F}_{ext} \tag{30}$$

ここで，$\boldsymbol{F}_{int}$及び$\boldsymbol{F}_{ext}$は混合体内部及び外部の，等価節点力，電解質溶液の等価節点電気化学ポテンシャル，節点における各イオンのmol数変化速度，非圧縮条件，電気的中性条件を表すベクトルである．

この式は非線形なので，増分分解してNewton-Raphson法を用い次の線形化方程式を反復的に解く．

$$\begin{bmatrix} \boldsymbol{P}_{11} & 0 & 0 & 0 & \cdots & \boldsymbol{P}_{1p} & 0 \\ 0 & 0 & 0 & 0 & \cdots & \boldsymbol{P}_{2p} & 0 \\ \boldsymbol{P}_{31} & 0 & \boldsymbol{P}_{33} & 0 & \cdots & 0 & 0 \\ \boldsymbol{P}_{41} & 0 & 0 & \boldsymbol{P}_{44} & & 0 & 0 \\ \vdots & \vdots & & & \ddots & 0 & 0 \\ \boldsymbol{P}_{p1} & \boldsymbol{P}_{p2} & 0 & 0 & \cdots & 0 & 0 \\ 0 & 0 & 0 & 0 & \cdots & 0 & 0 \end{bmatrix}^{(k)} \begin{Bmatrix} \Delta \boldsymbol{U}^{s(k)} \\ \Delta \boldsymbol{Q}^{w(k)} \\ \Delta C^{\mathrm{Na}(k)} \\ \Delta C^{\mathrm{K}(k)} \\ \vdots \\ \Delta P^{(k)} \\ \Delta \Psi^{(k)} \end{Bmatrix}$$

$$+ \begin{bmatrix} 0 & 0 & 0 & 0 & \cdots & 0 & 0 \\ 0 & \boldsymbol{G}_{22} & 0 & 0 & \cdots & 0 & 0 \\ 0 & \boldsymbol{G}_{32} & \boldsymbol{G}_{33} & 0 & \cdots & 0 & 0 \\ 0 & \boldsymbol{G}_{42} & 0 & \boldsymbol{G}_{44} & & 0 & 0 \\ & \vdots & & & \ddots & 0 & 0 \\ 0 & 0 & 0 & 0 & \cdots & 0 & 0 \\ 0 & 0 & \boldsymbol{G}_{e3} & \boldsymbol{G}_{e4} & \cdots & 0 & \boldsymbol{G}_{ee} \end{bmatrix}^{(k)} \begin{Bmatrix} \Delta \dot{\boldsymbol{U}}^{s(k)} \\ \Delta \dot{\boldsymbol{Q}}^{w(k)} \\ \Delta \dot{C}^{\mathrm{Na}(k)} \\ \Delta \dot{C}^{\mathrm{K}(k)} \\ \vdots \\ \Delta \dot{P}^{(k)} \\ \Delta \dot{\Psi}^{(k)} \end{Bmatrix}$$

$$= \boldsymbol{F}_{ext} - \boldsymbol{F}_{int(k-1)} \tag{31}$$

但し，右添え字kは反復計算の回数を表しており，ベクトルは節点での値を並べたものである．本研究では時間進行として後退Euler型時間積分アルゴリズムを適用して解を求めた．

3. 心筋細胞のモデル化

冒頭にも簡単に述べたが，心筋の収縮活動は，イオンの流れに支配される電気的活動をきっかけとする．図1は心筋細胞のイオンチャンネルと筋原線維周りの構造を模式的にあらわしたものである．以下，それぞれの要素の果たす役割を詳しく述べるとともに，心筋細胞の解析に三相理論を適用する方法について述べる．

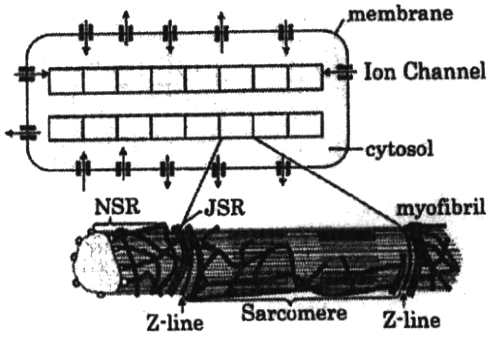

Fig. 1　Structure of cardiac cell

3·1 細胞膜

3·1·1 膜電流　細胞膜には蛋白複合体によって構成された複数種類の細孔(イオンチャネル)が存在している．イオンチャネルはそれぞれ決まった種類のイオンのみを通過させる，細胞内外の電位差(膜電位)などによってその透過性が変わる，ATPを使ってポンプのようにイオンを移動させる，などの特徴を持っている．これらの個々のイオンチャネルの特性を表した数理モデルは各種提案されている[8][10][11]．

細胞膜を通過する流れは全て細胞膜に垂直な方向に通過すると考えれば，膜垂直方向だけにノイマン境界条件を設定することで膜平行方向の流れを妨げることなくイオンチャネルの特性を三相理論に組み込むことができる．本研究ではten Tusscherら[8]によるヒトの左心室細胞のモデルにSAC(Stretch activated channel)電流を付加したモデル[9]を用い(ただし，SAC電流は細胞膜内での分布の偏りを考えて調整した)，またこのモデルで表されない水や塩化物イオンCl^-などは細胞膜を通過しないものとした．計算に用いる細胞内外の電位差(膜電位V_m)，イオン濃度は三相理論で計算した値を用いた．

3·1·2 膜電位　膜電流の数理モデルでは，各点においてキルヒホッフの第一法則(電気的中性条件と等価)が成り立つ，つまりイオンチャネルを通る電流の合計I_{ion}と容量電流の和が周りに流れ出す電流I_mと等しいことを用いて，膜電位V_mの時間発展と空間伝播を下記の式により計算する．

$$I_m = C_m \dot{V}_m + I_{\mathrm{ion}} \tag{32}$$

ここでC_mは単位面積当たりの膜の電気容量(膜容量)である．これらの値を今回のモデルへ適用するに先立ち従来の膜電流の数理モデルで使われている膜容量と

容量電流について詳しく議論する．一般に静的な状態では導体内部には電荷がなく導体の表面にだけ分布することが知られている．心筋細胞内部でも電気的中性条件により正負の電荷が打ち消しあい，余った電荷が膜付近に分布して膜電荷となると考えられる．この膜電荷に対しては膜を挟んで反対側，つまり細胞外部に異符号で同量の電荷が分布することで電気的中性条件を満たすと考えられる．ここで，微小領域についてだけみると，膜は平面であり膜電荷は一様に分布しているとみなせる．膜内には面に垂直な向きに一様な電界ができ，その強さ E はガウスの法則より $E = q/\varepsilon_0$ となる．ここで，q は単位面積あたりに蓄えられた細胞外の膜電荷，ε_0 は膜の誘電率である．膜の厚さを d とすると，膜電位 V_m は

$$V_m = Ed = \frac{qd}{\varepsilon_0} \equiv \frac{q}{C_m} \tag{33}$$

と表せて膜容量が定義される．容量電流は細胞外の膜電荷 q の変化率なので，従来の膜電流の数理モデルの式 (32) が得られる．

次に今回のモデルへの適用，つまり二相理論への組み込みについて述べる．今回のようにミクロな視点で見ると，膜電荷は実際には表面だけに分布するわけではなく，膜から離れるに従って 0 に近づいていく形で分布しており，単位体積あたりで表すべきと考えられる．そこで，膜に垂直な方向に積分することで C_m となる単位固体体積当たりの膜容量 $\tilde{C}_m$ を用いて単位体積あたりの膜電荷を $\tilde{C}_m V_m$ と定義する．細胞内の電荷の合計に細胞外の膜電荷を加えたものが，電気的中性条件を満足するという考えのもと，式 (9) において固定電荷を膜電荷を表す値に置き変え

$$\Phi^w \tilde{C}^F = \tilde{C}_m V_m \tag{34}$$

として計算を行った．細胞外では $\tilde{C}_m$ を逆符号として同様に変更した．

なお，今回膜電荷は細胞膜に接している要素内にのみ分布しているとして，$\tilde{C}_m$ を細胞膜にあたる節点の補間関数と同じ形の分布関数で定義した．式 (31) において $\boldsymbol{G}_{ve}$ が零行列になっていないのは，ここで膜電位 V_m が電位の関数で次のように表されることによる．

$$V_m = \psi_i - \psi_e = [N_{\psi m}]\{\psi_m\} \tag{35}$$

$\{\psi_m\}$ とは細胞膜の内側表面の節点と外側表面の節点での電位を並べたベクトルである．$[N_{\psi m}]$ は，膜の存在を考慮する要素では膜電位が二次元補間されるが，それ以外の要素では 0 になるように定義した．

3.2 筋小胞体のとりあつかい　細胞内には数本の筋原線維 (myofibril) が走っており，これらは約 1.8μm 毎に Z 帯 (Z-line) で筋節 (Sarcomere) とよばれる領域に区切られている．筋原線維は管が網状になっている網状筋小胞体 (NSR) と，Z 帯に沿って存在する接合筋小胞体 (JSR) という組織にくるまれている (図 1)．NSR と JSR をあわせて筋小胞体 (Sarcoplasmic Reliculum; SR) とよぶ．SR は内部に Ca^{2+} を蓄えることができる．興奮による細胞内への Ca^{2+} の流入などで Ca^{2+} 濃度が高くなると，これを引き金として JSR に蓄えられた Ca^{2+} が細胞内液へと放出される．細胞内液中の Ca^{2+} の一部は NSR に吸い上げられ，その後一部が JSR に移動し，一部は漏れ電流として細胞内液へと放出される．

SR を出入りする Ca^{2+} 電流については膜電流と同様に数理モデル化されているが，本論文では筋小包体形状を表せる程細かなメッシュを作成していないため，膜電流と同様に境界条件として与えることはできない．そこで，SR から流れ出す電流を Piola 変換したものを $\boldsymbol{J}^{\alpha}_{\mathrm{SR}}$ として式 (25) 左辺第三項の $\boldsymbol{J}^{\alpha}$ に加えた．この値は単位時間に SR から湧き出す電荷となり，従来の細胞生理モデルで計算できる値をそのまま用いることができる．本研究では NSR, JSR からの湧き出しとして，ヒトの左心室細胞のモデル[8]で計算した値 $I_{leak} + I_{up}$，及び Okada ら[2]によって用いられた I_{rel} をそれぞれ与えた．ただし，もとの細胞生理モデルの式は細胞内分布を考えず，細胞全体の平均としてイオン濃度を取り扱っているため，筋小胞体の分布を考慮してこれを修正した．なお，SR 内部で Ca^{2+} が NSR から JSR へと移動する過程は LR(Luo-Rudy) モデル[10][11]においてはモデル化されているが ten Tusscher のモデル[8]では NSR と JSR は区別されておらずその平均の値を用いているため，これにならって Ca^{2+} 濃度は同一 SR 内で瞬時に一様になるとした．

SR 内の電荷が細胞内液の電気的中性条件に与える影響については実験データが存在しないため，本研究では影響を与えるとして SR 内部の電荷を固定電荷として取り扱い，$\dot{C}_F = -\nabla_\chi \cdot \boldsymbol{J}^{\alpha}_{\mathrm{SR}}$ として与えた．

3.3 細胞内の Ca^{2+} バッファの取り扱い　筋原線維内部において，Ca^{2+} はトロポニン C というタンパク質と結合し，これをきっかけとして収縮力が発生する．細胞内液には Ca^{2+} と結合する calmodulin というタンパク質が存在し，Ca^{2+} の動きを妨げている．

タンパク質と結合した Ca^{2+} は自由に動き回ることができないが，電荷を持ち電気的中性条件に寄与するという点でやはり固定電荷である．従って SR に吸い